GEOPHYSICS, VOL. 89, NO. 5 (SEPTEMBER-OCTOBER 2024); P. L33–L48, 9 FIGS.
10.1190/GEO2023-0641.1

Tidally modulated seismic velocity changes observed using submarine dark fiber and the virtual-source method

Michal Chamarczuk[1], Jonathan Ajo-Franklin[2], Valeriia Sobolevskaia[2], and Jeremy Patterson[2]

ABSTRACT

Natural cyclical stress perturbations, including wet and solid earth tides, coupled with repeatable seismic monitoring approaches, provide a tool for understanding the elastic properties of rocks at depth. Ocean tides, in particular, perturb the overburden and pore pressure, affecting hydraulic and elastic rock properties. The recent emergence of distributed acoustic sensing (DAS) and seismology using existing dark telecom fiber offers an unprecedented opportunity to instrument the seas and oceans with seismic monitoring networks of large aperture, fine spatial resolution, and broadband sensitivity. We use a submarine dark-fiber array to methodologically assess whether the changes in seafloor seismic velocities are modulated by ocean tidal loading. Considering oceanic ambient noise (AN) in the frequency range between 1 and 5 Hz, we find it possible to retrieve reliable surface-wave estimates using relatively short time windows (approximately 60 min). Next, using the power of linear arrays to capture AN energy from the stationary-phase zones and AN processing techniques commonly used in DAS applications for subsurface monitoring in urban settings, we introduce a methodological approach to turn each segment of dark fiber into a short-offset monitoring array (2 km), providing redundant, hourly, surface-wave estimates. Using four days of AN data recorded by the Monterey Accelerated Research System (MARS) 20 km section offshore cable, we generate the virtual-source gathers for 10 segments spanning the whole MARS cable. We then use virtual-source data from one segment to estimate the hourly velocity changes that are then quantitatively compared with the tidal data. The results suggest that changes in seafloor seismic velocities are likely modulated by tidal height, even in regions without large tidal excursions. This advance demonstrates a new application of submarine telecom fibers for monitoring the seismic stress response of near-seafloor sediments.

INTRODUCTION

Monitoring seismic velocities allows geophysicists to analyze changes in the mechanical properties of the subsurface due to deformation, fluid flow, or temperature variations. These changes may be related to natural processes, such as fault deformation (Wegler and Sens-Schönfelder, 2007; Roux and Ben-Zion, 2014; Qiu et al., 2020) or volcanic activity (Ratdomopurbo and Poupinet, 1995; Sens-Schönfelder and Wegler, 2006; Obermann et al., 2013); alternatively, anthropogenic activities may generate similar impacts, e.g., hydrocarbon reservoir production (de Ridder and Biondi, 2013; de Ridder et al., 2014; Mordret et al., 2014) or carbon storage operations (Cheraghi et al., 2017; Issa et al., 2017; Stork et al., 2018). The measurement of natural cyclical forcings offers a path to calibrate these signatures by directly probing seismic sensitivity to poroelastic perturbations over time; examples include atmospheric forcings, solid and wet tidal effects, and seasonal water level variations, all of which can be used as tools to probe the nonlinear behavior of subsurface materials (Li and Ben-Zion, 2023). Monitoring the interaction between wet tidal loading and seismic velocities is of particular interest as it can provide near real-time information about seafloor sediment properties (Williams et al., 2019) and contribute to understanding how the seafloor reacts to the gravitational influence of ocean tides. Ocean tidal loading is the periodic deformation of the earth due to the weight and movement of surface fluids (Webb, 1986). Cyclical variations in sea level

---

Manuscript received by the Editor 25 October 2023; revised manuscript received 10 June 2024; published ahead of production 19 June 2024; published online 2 September 2024.

[1]Rice University, Department of Earth, Environmental, and Planetary Sciences, Houston, Texas, USA and Los Alamos National Laboratory, Los Alamos, New Mexico, USA. E-mail: chamarczukm@gmail.com (corresponding author).
[2]Rice University, Department of Earth, Environmental, and Planetary Sciences, Houston, Texas, USA. E-mail: ja62@rice.edu; vs46@rice.edu; jp128@rice.edu.

lead to changes in the elastic properties of the underlying rocks due to changes in lithostatic stress and pore pressure (Cutillo and Bredehoeft, 2011). As sea level rises, the increasing water column height compresses seafloor sediments and underlying formations, increasing elastic moduli. This loading effect can be counteracted by the increasing pore pressure, which expands the pore space and reduces sediment velocity. However, unlike the relatively rapid loading effect, the pore pressure gradually diffuses through the rocks, controlled by sediment permeability. As a result, these two competing processes might have different effects at different depths (Reasenberg and Aki, 1974). Quantifying the dynamic interaction between seismic velocities and ocean tidal loading requires ambient noise (AN) analysis and Scholte wave inversions with a high temporal resolution to capture diurnal and semidiurnal tidal excursions. However, if available, this class of measurements provides a window into the small strain poroelastic response of seafloor formations and potentially near-seafloor permeability, which can be derived from the temporal lag in the pore pressure impacts.

Recently, the application of distributed acoustic sensing (DAS) has revolutionized researchers' capacity to conduct environmental studies using dense broadband seismic recordings that are continuous over long periods (Ajo-Franklin et al., 2019; Zhan, 2019; Lindsey et al., 2020). DAS measurements take advantage of Rayleigh backscattering, using laser pulses injected into the fiber to measure the strain or strain rate along its length (e.g., Dou et al., 2017; Lindsey et al., 2017). This allows for the continuous acquisition of seismic data with meter-scale spatial resolution across distances of tens of kilometers (Daley et al., 2013, 2016), effectively turning the fiber optic cable into a 1C broadband strain-rate sensing array (Lindsey et al., 2017).

Although DAS measurements can be conducted on fit-for-purpose fiber optic cables, another approach is to use the unlit fibers present in preexisting telecommunication cables already installed in the subsurface (including the existing submarine cables). These fibers, referred to as "dark fibers," circumvent the expensive process of deploying fit-for-purpose fiber sensing networks (Jousset et al., 2018; Ajo-Franklin et al., 2019). Cables with dark fiber are widespread across the continental United States as a part of the international telecommunication network and are often available to be leased or purchased from commercial providers. Several studies have shown that combining dark-fiber DAS and continuous recordings allows for monitoring using various parts of recorded seismic wavefields: the P waves of quarry blasts (Fang et al., 2020), surface waves generated by traffic and other urban AN sources (Ajo-Franklin et al., 2019; Shragge et al., 2021; Czarny et al., 2023; Yang and Shragge, 2023), surface-wave coda (Rodríguez Tribaldos and Ajo-Franklin, 2021), or surface waves generated by earthquakes (Yu et al., 2019). A common characteristic of several urban DAS studies using surface waves is combining dark-fiber infrastructure for the acquisition and various modifications of seismic interferometry (SI) techniques for processing. Here, we repurpose this combination by using oceanic AN (OAN) DAS data to monitor changes in Scholte wave velocity in a marine setting.

Apart from having a substantial onshore footprint, there are more than 350 active submarine cables worldwide, spanning 1.2 million km. Due to the challenging logistics and costs associated with ocean deployment (see Williams et al., 2019), most permanent broadband seismic stations are situated on land, thereby positioning dark-fiber DAS technology as a powerful instrument for seafloor monitoring studies.

Recent studies using DAS on submarine cables have yielded promising results in terms of data quality (Lindsey et al., 2019; Williams et al., 2019). These studies successfully detect local and teleseismic events, along with microseism noise and other oceanic signals across a wide frequency spectrum (Lindsey et al., 2019; Sladen et al., 2019; Lior et al., 2021). Several DAS investigations on submarine cables demonstrate that seafloor dark fiber can be effectively used for Scholte wave imaging (Cheng et al., 2021; Spica et al., 2022; Viens et al., 2023), localizing unmapped fault zones (Lindsey et al., 2019), and monitoring ocean surface gravity waves (Williams et al., 2022). The recent works by Spica et al. (2022) and Viens et al. (2023) underscore the significant passive imaging potential achieved through the fusion of seafloor DAS with earthquake (Spica et al., 2022) and AN recordings (Viens et al., 2023). To further advance submarine DAS studies, Romanowicz et al. (2023) recently introduce a real-time seafloor monitoring experiment targeting a range of seismological objectives and spanning more than one year of continuous data acquisition. Our study builds on previous submarine DAS efforts (Lindsey et al., 2019; Spica et al., 2020, 2022; Cheng et al., 2021; Lior et al., 2022; Williams et al., 2022; Viens et al., 2023) and studies showing that onshore DAS arrays using communication infrastructure are suitable for subsurface monitoring in urban settings (Dou et al., 2017; Ajo-Franklin et al., 2019; Fang et al., 2020; Rodríguez Tribaldos and Ajo-Franklin, 2021; Shragge et al., 2021; Yang and Shragge, 2023).

We focus on combining the capacity of DAS for monitoring and its unprecedented potential to instrument the ocean. Using dark fiber, the spatiotemporal persistence of OAN (Webb 1986; Webb et al., 1991), and state-of-the-art AN processing techniques such as phase-weighted stacking (PWS; Schimmel and Paulssen, 1997) and bin stacking (Nakata et al., 2015), we propose an efficient solution for monitoring near-seafloor seismic velocity changes induced by tidal forcings. We start with a brief review of the seafloor seismic velocity monitoring requirements and formulate the motivation behind our newly developed monitoring scheme. Next, we explain the processing workflow for generating dark-fiber virtual-source gathers (VSGs) for monitoring, demonstrate the results of individual processing steps, and highlight the time convergence of the virtual-source data needed to retrieve the surface waves necessary for monitoring. To test the methodology, we apply our processing to the Monterey Accelerated Research System (MARS) submarine dark-fiber data sets (Lindsey et al., 2019; Cheng et al., 2021; Romanowicz et al., 2023) and generate high-quality VSG for short linear subarrays spanning the whole cable. Next, we choose one segment and use it to demonstrate the possibility of hourly dark-fiber seafloor monitoring of the velocity changes that correlate with high- and low-tide oscillations. Although the focus of our work is on methodological development, the key finding is the observation of tidally modulated changes of seafloor seismic velocity; this observation, coupled with appropriate interpretive models, provides a portal into the poroelastic stress response of seafloor sediments.

MONITORING CONSIDERATIONS

A variety of prerequisites should be satisfied to allow confident analysis of time-variant seismic signals in the context of probing the impact of natural forcings. Ideally, the recorded time-lapse seismic velocities should exclusively capture the time-lapse signals stemming from alterations in the elastic parameters within the desired subsurface target zone (Nakata et al., 2022) in contrast with the changes in the noise field. They should be free of any extraneous variations, such as those arising from modifications outside the target zone or nonreproducible acquisition influences (Almagro Vidal et al., 2019; Mao et al., 2020; Qin et al., 2022; Yang and Shragge, 2023). This suggests that a permanent sensing network will be beneficial alongside processing tools that yield consistent results regardless of variations in recorded data not related to the subsurface (Ajo-Franklin et al., 2022; Yang and Shragge, 2023). Having access to the permanent (fixed infrastructure) dark-fiber acquisition allows for consistent data recording within the same subsurface zone (Ajo-Franklin et al., 2019). Together with the spatiotemporal coherency of the OAN observed at various scales (Webb, 1986; Webb et al., 1991), it is reasonable to consider combining continuous submarine dark-fiber acquisition with SI techniques, although not all of these constraints are fulfilled in practice. SI with AN allows the use of passive seismic sources (i.e., sources not generated for the purpose of seismic acquisition) to monitor the changes in the subsurface that may occur over time (e.g., Snieder and Hagerty, 2004; Snieder, 2006; Brenguier et al., 2016).

Due to the variations in natural seismicity, the main challenge in passive seismic analysis is producing repeatable results (e.g., Almagro Vidal et al., 2019). Considering monitoring methods that rely on AN processing involving correlation techniques, we can distinguish two main methodological approaches: single-station (autocorrelation) (Claerbout, 1968; Daneshvar et al., 1995) and interstation approaches (crosscorrelation [CC]) (Wapenaar, 2003; Bakulin and Calvert, 2004; Schuster et al., 2004). Both methods are affected by similar limitations: the frequency bandwidth used for analysis and the variability of the waveforms generated by the AN sources. Recently, Li and Ben-Zion (2023) propose an efficient deconvolved autocorrelation approach that allows for the mitigation of spectral variations in background noise by using vertical and horizontal components of the recorded AN. However, as mentioned previously, dark-fiber DAS, although providing a large number of channels, records only a single wavefield component inline with the fiber orientation. Fortunately, one major advantage of the interstation approach is the possibility of using the recording of one station to deconvolve the source imprint of the other (e.g., Snieder et al., 2009; Nakata et al., 2011), for instance, by using deconvolution interferometry (Vasconcelos and Snieder, 2008) or crosscoherence (Nakata et al., 2011) approaches. From the monitoring perspective, the downside of the CC-based methods is the necessity of stacking the recorded AN over time to enhance the signal-to-noise ratio (S/N) (Draganov et al., 2009, 2013; Issa et al., 2017; Rodríguez Tribaldos and Ajo-Franklin, 2021; Yang and Shragge, 2023), often resulting in a time resolution of days to months. To achieve the temporal resolution necessary to capture the potential signal variability related to tidal loading, it is necessary to achieve a faster convergence rate of the SI results. For instance, Rodríguez Tribaldos and Ajo-Franklin (2021) demonstrate that with proper processing (including spectral whitening and PWS), the coda-wave component of the ambient wavefield recorded by the dark fiber deployed in an urban setting may be used to retrieve high-quality hourly virtual-source products allowing for reliable velocity estimates, and thus, also allowing for the monitoring of diurnal or semidiurnal processes.

One notable aspect of onshore dark-fiber DAS is that their deployment often uses the “right-of-way” corridors along roads and rail connections, which are typically rich in ambient seismic noise (Ajo-Franklin et al., 2019). This is not the case for seafloor cables, for which the deployment strategy and noise environment vary significantly depending on the location (e.g., Spica et al., 2020, 2022). Close to the coastline, cables are typically trenched at shallow depths, whereas in the deeper sea, they are laid directly on the ocean floor. This implies differences in coupling for individual segments of dark fiber, as well as local differences between recorded AN due to characteristic interactions between oceanic waves and varying seabed topography. Even though it has relatively consistent deployment conditions, onshore dark-fiber DAS is also prone to having zones of coherent anthropogenic sources dominating the various segments along the cable (e.g., Ajo-Franklin et al., 2022). Cheng et al. (2023a) develop a methodology based on combining PWS and bin stacking to attenuate the effects of such persistent noise sources. We identify an analogy in tackling the effects of different persistent sources across dark fiber deployed in urban areas and improving the coherency of surface waves retrieved in VSGs for different segments of submarine dark fiber. We focus on developing the coherency-improvement methodology required to produce repeatable virtual-source data for each segment along seafloor dark fiber.

Recently, an offshore DAS study by Williams et al. (2022) shows that it is possible to use OAN (specifically surface gravity waves) in the frequency range (<0.1 Hz) to generate virtual-source data for velocity monitoring of ocean currents. As a coherency-improvement technique, Williams et al. (2022) use *f-k* filtering, which is efficient in separating wavefields based on their directionality (e.g., separating the seaward and landward propagating wavefields). This method requires careful parameterization; otherwise, it may be prone to numerical artifacts in the presence of poorly coupled channels and tends to smooth the resulting virtual-source data artificially. As a result, this method seems more applicable for static imaging studies rather than monitoring campaigns, which require processing solutions that can be parameterized once in the beginning of the monitoring campaign. Of particular relevance to this study, Viens et al. (2023) demonstrate the extraction of multimodal surface waves from continuous DAS recordings and use them for estimating the shallow S-wave velocity (V_S) structure along the cable. The primary coherency-improving technique used in Viens et al. (2023) is one-bit normalization, recognized for its effective balance between mode separation and lateral spatial resolution. In our study, the focus lies more on the temporal stability of the results, aiming to use a single mode of surface waves. Therefore, as elaborated in the subsequent sections, the methodology in this study relies on trading space for time, thereby enhancing temporal resolution at the expense of spatial information.

In this study, we use surface waves present in the previously unused part of the OAN frequency spectrum (>0.5 Hz) and explore temporal variations related to the subsurface. In the next sections, we detail our processing strategy for monitoring subsurface seismic properties using submarine dark fibers. We focus on the development of an easily automated suite of algorithms that might be deployed in a range of offshore environments for seafloor seismic velocity monitoring. We demonstrate the approach using a previously acquired data set from Monterey Bay, CA, which is the topic of prior studies; analysis of the data set demonstrates the sensitivity of Scholte waves to tidal forcing in this context. We end by exploring some of the problems that similar natural forcings might allow access to.

DATA AND METHODS

Data

The DAS data evaluated in this study were recorded on the MARS science cable, located on the continental shelf offshore of California, north of Monterey Canyon (Figure 1). The goal of the initial MARS DAS deployment was to investigate the utility of seafloor DAS recordings for various marine geophysical studies. The experiment details and acquisition campaign were described in Lindsey et al. (2019) with follow-up analysis performed by Cheng et al. (2021); we summarize the network geometry for clarity but refer the interested reader to the previous papers for greater detail. The MARS data set used in this study consisted of four days of continuous passive DAS measurements acquired between 10 and 13 March 2018. A Silixa iDAS v2 interrogator unit was connected to one end of the fiber at the MARS shore terminus station (Lindsey et al., 2019), and the MARS cable was buried approximately 0.9 m below the sea floor along most of its route. The recording consisted of 10,000 channels (2 m channel spacing) along a 20 km single-mode dark fiber inside the MARS cable, with a gauge length of 10 m and a sampling frequency of 1 kHz. Continuous recordings were stored in 1 min segments in TDMS format, with each record approximately 600 MB in size. The MARS data set was first used to demonstrate the potential for using seafloor DAS for regional seismic event detection, locating unmapped fault zones with earthquake recordings (Lindsey et al., 2019), and, subsequently, for accurate fault-zone imaging using high-resolution 2D S-wave velocity profiles (Cheng et al., 2021). Here, we focus on investigating the potential of this data set for surface-wave velocity monitoring and report the tidally modulated seismic velocity changes.

Methods

The initial processing workflow for measuring seismic velocity changes using dark fiber and virtual sources consists of three main processing steps schematically represented in Figure 2: the segmentation of the dark fiber into shorter subarrays (Figure 2d), application of the SI workflow to all the channels belonging to the given segment (Figure 2e), and spatial stacking (Figure 2f), which combines all VSGs from a given segment into a single improved VSG. Using stacked VSGs, the velocity changes between the stacking epochs can be estimated for either the ballistic phases or coda components.

Before the main processing steps indicated previously, we apply a four-step preprocessing sequence to the MARS recordings: (1) removal of the mean and trend, (2) band-pass filtering (0.5, 1.0, 4, and 5 Hz), (3) temporal decimation (from 1 kHz to 12.5 Hz), and (4) spatial median filtering and spatial decimation from 10,000 channels with a 2 m interchannel distance to 1000 channels with a 20 m interchannel distance. This preprocessing sequence allows us to enhance the surface-wave energy not related to the ocean surface gravity waves typically dominating OAN recordings below 0.5 Hz (Guerin et al., 2022; Williams et al., 2022). The decimation steps also dramatically decrease the computational cost because the input data dimension is reduced by 80 and 10 times in the temporal and spatial dimensions, respectively.

Array segmentation

In this study, the segmentation of the dark-fiber cable for velocity monitoring involves dividing the entire length of the cable into N segments of equal length. Each segment acts as an independent linear array, which can be used separately for velocity monitoring. The general formula for calculating the length of each segment (L_{segment}) is given by

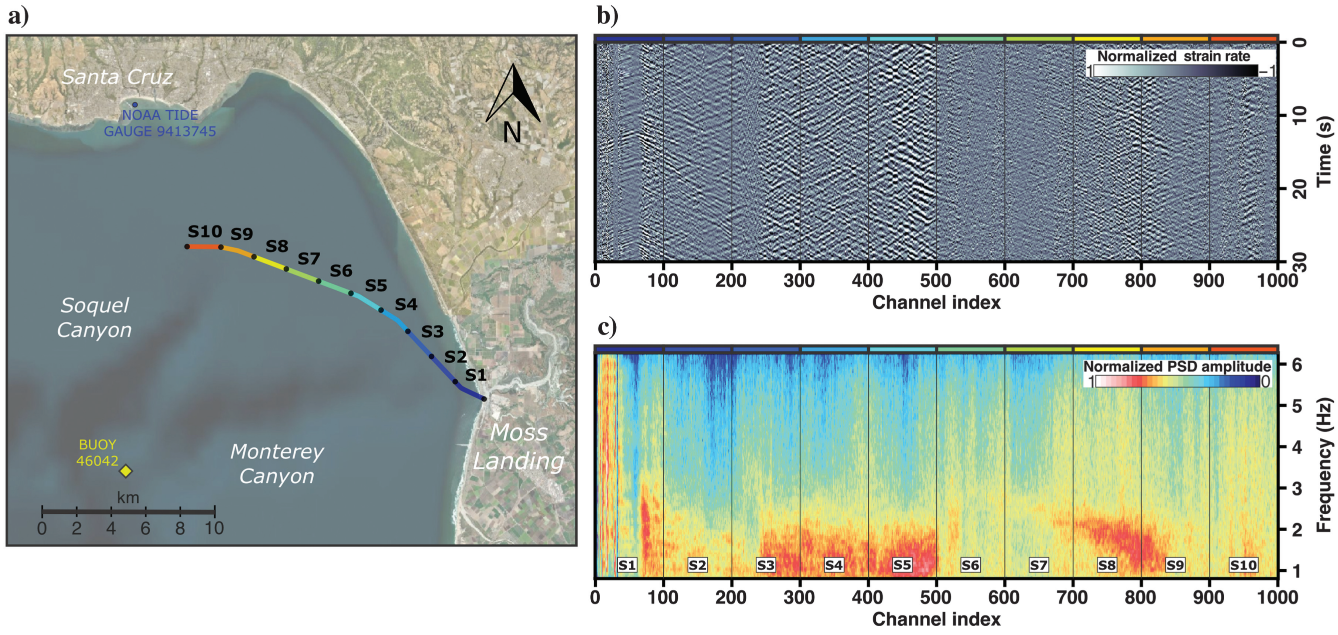

Figure 1. (a) Location of the DAS cable (the colored lines) used for observing the AN at Monterey Bay, CA; the segmentation of the cable (denoted by black dots and the letter "S") into 2 km long subarrays; and NOAA buoy 46,042 (the yellow diamond). (b) Typical 30 s OAN record of the strain rate along the 20 km fiber optic cable. (c) The power spectral density of the record shown in (b).

$$L_{\text{segment}} = \frac{L_{\text{Total}}}{N}, \tag{1}$$

where L_{Total} represents the total length of the dark-fiber cable and N is the number of desired segments. In general, segmentation of the dark fiber for monitoring purposes should be done based on the local AN conditions or can be done arbitrarily by dividing the cable into segments of equal length, with the latter approach facilitating sequential array processing (i.e., the same number of channels in each segment). In such cases, the main factor governing the length of the segment is the spatial extent to which the coherency of the surface wave emerging from the single source can still be observed, which is determined by the strength and distribution of the AN sources in the area of study (e.g., Cupillard and Capdeville, 2010) and the processing strategy (e.g., Liu et al., 2023). For OAN (Cheng et al., 2021; Guerin et al., 2022; Viens et al., 2023), the recorded wavefield contains a mixture of different modes, and it is difficult to spatially separate the overlapping sources, for instance, by identifying the persistent sources typical for urban areas (e.g., Czarny et al., 2023). As a result of this ambiguity, we divide the total cable length into N equal segments. To determine the range of channels falling within the kth segment (where k ranges from 1 to N), we use the following formulas: the lower channel number (C_{lower}) for the kth segment as $C_{\text{lower}} = (k-1)(C_{\text{Total}}/N) + 1$ and the upper channel number as $C_{\text{upper}} = k(C_{\text{Total}}/N)$, where C_{lower} is the lowest channel number within the kth segment, C_{upper} is the highest channel number within the kth segment, k is the segment number (ranging from 1 to N), C_{Total} is the total number of available channels in the dark-fiber cable, and N is the number of desired segments.

For the MARS cable case, we use the following values ($L_{\text{Total}} = 20$ km, $C_{\text{Total}} = 1000$, and $N = 10$ segments) to calculate the channel group falling within each segment. The length of each segment is 2 km, and the channels falling within the kth segment are $C_{\text{lower}} = (k-1)100 + 1$ and $C_{\text{upper}} = (k)100$. In this way, the MARS dark fiber, which, after spatial resampling, consists of 1000 channels, is distributed evenly across the 10 segments, each covering a range of 100 channels.

Empirical Green's function retrieval

To obtain the empirical Green's function (EGF) used as input for seismic velocity monitoring, we apply an AN processing workflow consisting of preprocessing, crosscorrelation, and PWS. The basic algorithm for EGS retrieval uses the crosscorrelation of cotemporal recordings between stations, an approach that has been shown to be a good approximation of the Green's function of the medium between these two stations (Weaver and Lobkis, 2001; Snieder, 2004; Wapenaar and Fokkema, 2006), assuming an isotropic distribution of the noise sources. The trace obtained through SI corresponds to the wavefield that would have been registered at one of the receivers if there had been a source located at the position of the other receiver (Wapenaar et al., 2004). This method does not necessitate an actual source at either receiver, leading to the adoption of the term "virtual source" to differentiate it from real seismic sources.

We apply the following EGS retrieval approach for every receiver inside an analyzed segment. We use the spectrally normalized crosscorrelation approach described by Nakata et al. (2011). Spectrally normalized crosscorrelation between receivers A and B recorded at time interval t can be defined as

$$C_{\text{Ch}}(x_B, x_A, \omega) = \sum_{t=1}^{N} \frac{u_t(x_B, \omega)\, u_t^*(x_A, \omega)}{|u_t(x_B, \omega)||u_t(x_A, \omega)| + \epsilon}, \tag{2}$$

where $u_t(x_A, \omega)$ and $u_t(x_B, \omega)$ are the AN recordings in the frequency domain ω observed at time interval t, at receiver x_A and x_B, respectively, $*$ is a complex conjugate, and ϵ is a regularization parameter used for numerical stability (Nakata et al., 2015). The spectral division in equation 2 cancels the influence of the source, making the results less dependent on the source signature. This operation is then repeated for each recorded time interval (here, 1 min). For each recorded 1 min noise panel, equation 2 is computed between a receiver, acting as a master trace, and every other receiver from the currently analyzed segment. Crosscorrelating a single DAS channel acting as a master trace with every other channel along the segment yields VSGs as if the shot were acquired at this master trace location. This procedure is performed for each analyzed noise panel, and after processing the amount of data equal to the monitoring time step, the process is repeated for the next master trace along the segment until all channels from a given segment are used as a master trace.

After assembling VSGs for n time windows, VSGs with the collocated virtual sources are stacked together using PWS. To obtain the phase-weighted stack, we use the phase coherency of the signal:

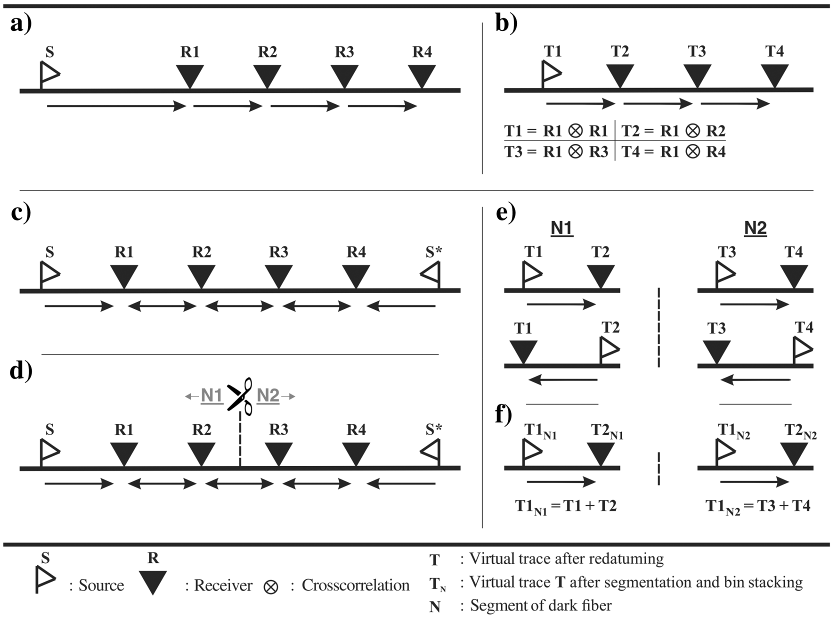

Figure 2. Diagrams of the source-receiver transformations used for (a and b) a conventional SI configuration and (c–f) an SI with a segmentation approach. (a) Interreceiver geometry, (b) VSG retrieved for the geometry in (a), (c) interreceiver geometry for the linear array illuminated from the sources on both ends, (d) segmentation of the receiver array into segments of equal length, (e) VSGs retrieved for subarrays in (d), and (f) improved VSGs retrieved from spatially combining VSGs in (e).

$$c(t) = \frac{1}{N}\left|\sum_{k=1}^{N} \exp[i\phi_k(t)]\right|, \tag{3}$$

where N is the number of receivers, i represents the imaginary unit, and $\phi_k(t)$ is the instantaneous phase of the analytic signal recorded at the kth receiver. The PWS is obtained by multiplying the real signal with the coherency component:

$$s(t) = \frac{1}{N}\sum_{k=1}^{N} x(\mathrm{t})_k c(t)^{\upsilon}. \tag{4}$$

The exponent υ controls the contribution of each sample to the stack with a decreasing value of c (i.e., attenuating the incoherent signals, often related to the sources in the nonstationary zones in the AN studies, e.g., Melo et al., 2013). In general, increasing υ yields a higher S/N in the resulting stacks, but using too high a value can distort the signal. Here, we use $\upsilon = 2$, which, as shown by Schimmel and Paulssen (1997), is often an optimal choice for the processing of array data. The PWS is performed over k traces, where each trace corresponds to the collocated trace in the collection of VSGs (for the same master trace) obtained for consecutive time windows. PWS is repeated for every virtual-source position along the segment (i.e., only VSGs with the same master trace are stacked together).

Spatial stacking

The final step in generating virtual-source data for monitoring is the spatial summation of all VSGs retrieved in the previous step. Spatial bin stacking in SI applications involves dividing the data into spatial bins and summing the data from multiple offsets within each bin (e.g., Nakata et al., 2015; Chmiel et al., 2019; Cheng et al., 2023a). This technique is commonly used to enhance the S/N and extract coherent energy from the VSGs. We denote the source-receiver offset as x and the virtual-source data recorded at a source location x_s, for a specific source-receiver offset x as $\mathrm{VSG}(x_s, x)$. The stacked data, denoted as $\mathrm{VSG}_{\mathrm{stack}}(x_k)$, can be obtained by summing the data within a spatial bin centered at x_k:

$$\mathrm{VSG}_{\mathrm{stack}}(x_k) = \sum_{x_s} \sum_{x\in\left[x_k-\frac{\Delta x}{2},x_k+\frac{\Delta x}{2}\right]} \mathrm{VSG}(x_s, x). \tag{5}$$

The summation is performed over all VSGs and all source locations. Here, x_k represents the center of the kth bin and Δx is the width of each bin. The size of the bin is typically determined based on the desired spatial resolution and sampling interval along the offset axis. The number of traces falling within the bin centered at x_k can be computed using the following equation:

$$N_{\mathrm{BIN}}(x_k) = \sum_i f_k[x(i)], \tag{6}$$

where x is the source-receiver offset variable. The indicator function $f_k(x)$ determines which trace falls within the kth bin by assigning one to these traces:

$$f_k(x) = \begin{cases} 1, & |x - x_k| \le \frac{\Delta x}{2} \\ 0, & \text{otherwise} \end{cases}. \tag{7}$$

We can use the indicator function $f_k(x)$ as a selector to decide whether a trace for a given receiver in a given VSG should be included in stacking, and the summation can be expressed as

$$\mathrm{VSG}_{\mathrm{stack}}(x_k) = \sum_i \mathrm{VSG}[i, x(i)] * f_k[x(i)]. \tag{8}$$

By summing up the indicator function for all receiver locations i, we can determine the number of traces falling within each spatial bin. Note that this equation assumes a continuous range of offsets. In practice, the actual number of traces falling in a bin may depend on the discretization of the offset values and any additional criteria or data selection applied during the binning process.

To compute all bin centers for spatial bin stacking, we need to define the size of each bin and the desired spatial resolution. We can denote the center of the kth bin as x_{k_center} and the size of each bin as Δx. The equation to compute the bin centers can be expressed as $x_{k\_\mathrm{center}} = x_{\min} + (k - 0.5) * \Delta x$, where k ranges from 1 to N and N is the total number of bins. Here, $x_{\min}$ represents the minimum source-receiver offset of interest and Δx represents the size or width of each bin. The inclusion of 0.5 in the equation is to ensure that the center of each bin falls in between the boundaries of the adjacent bins. This is necessary to evenly distribute the bins along the offset axis. Spatial bin stacking is performed on all VSGs obtained after PWS and repeated for each time step of monitoring. We use a bin size equal to double the channel spacing, which is equal to 40 m for this particular survey. The final product of the processing described in this section forms an input to compute the dispersion spectrum, which is used for velocity picking.

APPLICATION TO SUBMARINE DARK-FIBER DAS DATA

In this section, we analyze four days of continuous MARS submarine DAS recordings to obtain virtual sources along 10 subarrays. Next, we use one of the segments to generate hourly high-coherency VSGs, which we use to estimate the velocity changes that appear to be correlated with the available ocean tide data, thus demonstrating the sensitivity of this class of AN measurements to natural hydraulic forcings.

Time convergence of virtual-source data

One of the primary factors determining the quality of time-lapse virtual-source data is the amount of AN stacking required to retrieve high-quality surface waves in the EGF (e.g., Draganov et al., 2013; Nakata et al., 2015; Olivier et al., 2015; Issa et al., 2017; Thangraj and Pulliam, 2021; Yang and Shragge, 2023). Consequently, the minimum amount of data sufficient to achieve coherent surface waves determines the temporal resolution of the seismic velocity changes that might be measured. For natural forcings with diurnal or semidiurnal periods, temporal epoch lengths on the scale of hours are required to sample the resulting seismic response effectively.

OAN in the Monterey Bay area illuminates the array from a broad range of angles (Cheng et al., 2021) and, thus, allows us to produce the VSG with surface waves traveling in various directions depending on the position of the master trace (compare the rows in Figure 3a). Here, we use VSG data from segment 3 (which extends approximately 4–6 km from the shore), located at the position of the first master trace (the leftmost column in Figure 3a), and investigate the improved quality of the retrieved surface waves as a function of the AN stacking periods. In Figure 4a, we show the resulting VSGs, and in Figure 4b, we show the evolution of a single monitored trace denoted by a vertical black line in Figure 4a. The green traces denote the results for the time intervals from VSGs in Figure 4a. The time convergence, shown as an increase in the S/N in Figure 4b, is measured as the logarithm of the ratio between the maximum amplitude in the time window around the surface-wave arrival (the signal window) and the remaining part of the trace (the noise window). The division of the trace between the signal and noise windows is denoted by the horizontal black lines in Figure 4a. The notable effect of oceanic noise on SI results is an almost linear improvement of the S/N with increasing stacking time (denoted by the blue line in Figure 4b) out to approximately 1 h. In the MARS data, ballistic Scholte wave arrivals reach convergence in approximately 50–60 min, which justifies analyzing the velocity within 1 h intervals. For comparison, the last VSG shown in Figure 4a represents VSG obtained using 24 h of data, which exhibits quality comparable to the results obtained using 50–60 min of AN, thereby suggesting minimal improvement of S/N with stacking amounts of data beyond 1 h.

Selection of the segment for monitoring

The premise of the methodology described in this study is the ability to leverage existing dark fiber into multiple densely sampled monitoring subarrays. In this subsection, we explore whether the processing strategy shown in Figure 3 is sufficiently redundant to produce high-quality virtual sources for all segments indicated in Figure 1a. From the processing point of view, the main motivation behind segmenting dark fiber into subarrays is to enhance the natural coherency of local AN sources. For instance, in the VSGs obtained using between 1 and 20 min of data, as shown in Figure 4a, we can see that the main wavefront of the retrieved surface waves reaches approximately half of the analyzed segment (near the 50th trace indicated with a vertical black line, corresponding to the source-receiver offset of 1000 m). By using more data, and with careful processing, it is possible to retrieve surface waves traveling across the whole length of the segment. For reference, in Figure 4, note the coherent wavefronts of the surface waves traversing the whole length of the segment for VSG obtained from 50 min (and above) of the data.

As mentioned previously, we divide the 20 km long part of the MARS cable shown in Figure 1 into 10 2 km long subarrays denoted with the letters S1–S10 in Figure 1a. For each part of the cable, we repeat the same processing sequence: (1) segmentation, (2) spectral whitening, (3) band-pass filtering, (4) crosscorrelation, (5) PWS, and (6) spatial binstacking. Repeating this procedure for 10 segments results in the high-coherency VSGs, as shown in Figure 5. The improved coherency VSGs exhibit highly coherent ballistic Scholte wave arrivals traversing the whole 2 km extent of each segment. Due to the same processing being applied to each segment and the similar apparent velocities of the dominant arrivals (the dominant arrivals in each segment fall inside the range of apparent velocities >250 and <500 m/s), we interpret the differences between the segments as related to variations in the local subsurface. For instance, Scholte waves retrieved for segments 5 and 8 (Figure 5) are interpreted as results of body-wave conversion at subvertical seafloor faults (Lindsey et al., 2019; Cheng et al., 2021), which further confirms the sensitivity of small dark-fiber subarrays to the local geology. In this study, we focus on tracking velocity changes; for monitoring, we choose the segment for which the virtual-source pattern consists primarily of the single dominant type of surface wave and, thus, is not prone to additional source effects.

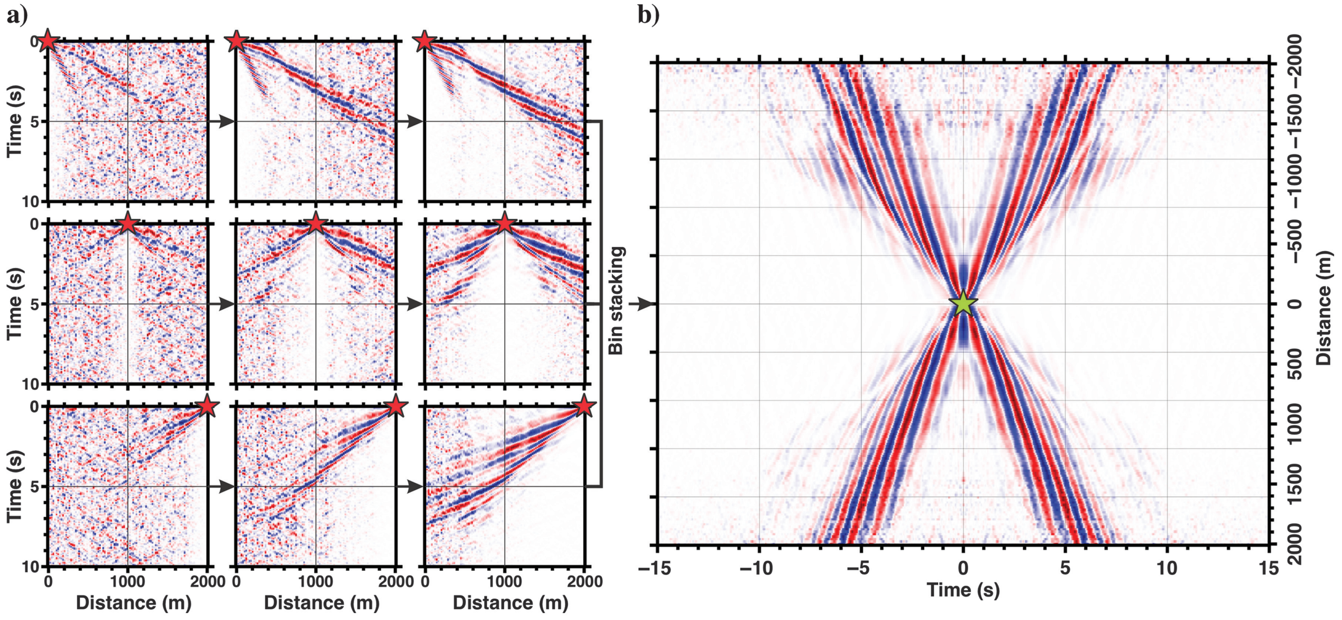

Figure 3. Performance of the processing scheme for retrieving the improved-coherency VSGs using a single subarray (segment S3) of the MARS DAS cable. (a) VSGs obtained using master traces located at the beginning (the top row), middle (the middle row), and end of the segment (the bottom row). Each column represents VSGs obtained at the same master-trace position with an increasing amount of AN data (from left to right: 15, 30, and 60 min; the number of minutes corresponds to the number of noise panels used). (b) Bin-stacked VSG obtained from spatially combining VSGs obtained at every second receiver acting as master along segment 3.

Seismic velocity monitoring

In this section, we use segment S3 (Figure 5) to examine the seismic velocity changes that occurred during the acquisition campaign. We compute the dispersion spectra from the hourly high-coherency VSGs; for each analyzed hour, we pick the phase velocities corresponding to the highest energy in the dispersion spectrum for all frequencies between 1.9 and 2.1 Hz. Tracking this response is a sensitive approach for monitoring the velocity changes in ballistic Scholte waves sampling the same subsurface volume. We pick the velocities of a mode interpreted to be the fundamental Scholte wave mode, although higher overtones are also visible, as shown in Figure 6b. In Figure 6a, we show the resulting seismic velocity curve as a function of calendar time. The error bars correspond to the minimum and maximum picked phase velocity over the analyzed frequency range. The semidiurnal periodic behavior of the velocity changes suggests its dependence on the tidal forcing. Indeed, as shown in Figure 6b, we observe that the Scholte wave velocity appears to be tidally modulated (the green line in Figure 6b) with maximum excursions of approximately 15 m/s over the four-day observation period. The observed changes in the phase velocity curve positively correlate with high and low tides. The peaks and troughs of the observed velocity changes generally agree with the peaks and troughs of the tidal data. However, the values of the velocities between the subsequent peaks and troughs are not consistent, thus suggesting additional forces contributing to the variability. In particular, we observe a high-amplitude seismic velocity anomaly between 02:00 and 17:00 on 11 March, whereas the wet tide variations are similar in magnitude during the experiment. The wet tide measurements (tide gauge) are recorded by a water level monitoring station in Santa Cruz, CA (a National Oceanic and Atmospheric Administration [NOAA] tide gauge of 9413745 as denoted in Figure 1a), located approximately 15 km from the S3 subarray of the MARS cable.

In Figure 7, we further inspect the picked seismic phase velocities and compare the result with several other environmental measurements. In Figure 7a, we show the measurement uncertainty

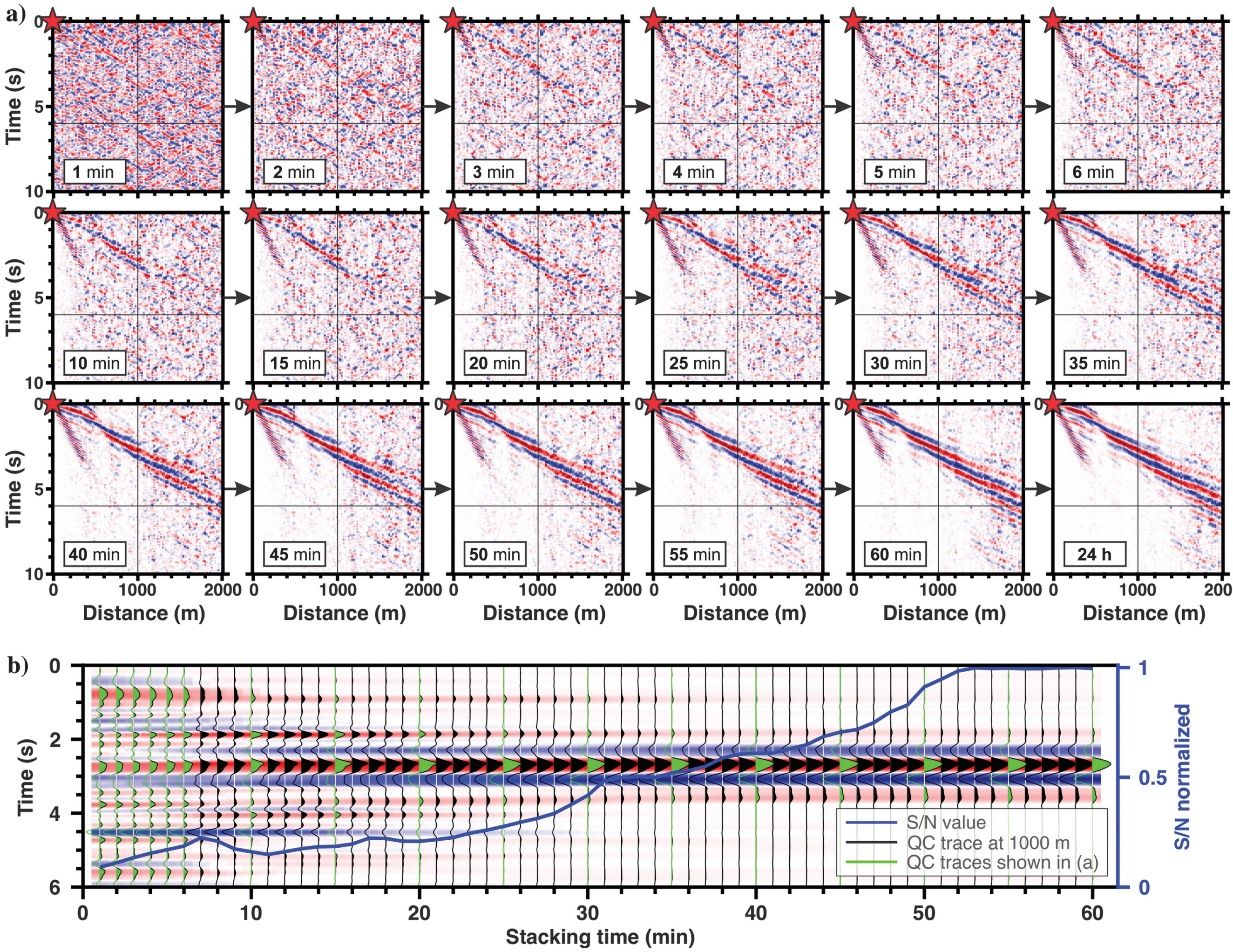

Figure 4. Influence of using more AN data for the retrieval of VSGs using segment S3 of the MARS DAS cable. (a) Evolution of the surface waves retrieved using SI applied to a single master-trace position, using gradually longer recordings of OAN. The inset in each panel denotes the amount of AN data used for processing. The horizontal black lines correspond to the division between the signal and noise windows used for the S/N calculation. (b) Single trace analysis of the S/N (denoted by a blue line) at offset 1000 m (denoted by a vertical black line in [a]) for VSGs obtained using an increasing amount of AN. Black wiggle traces show the traces for 60 stacking times between 1 and 60 min with 1 min intervals. Green wiggle traces correspond to the VSGs shown in (a).

calculated as three times the standard deviation of the difference between the actual velocity picks and the smoothed velocity curve (the blue line in Figure 7a), plotted against the actual velocity picks. The magenta bars in Figure 7a indicate the time intervals when the data quality was not sufficient for the computation of VSGs (due to the pauses in the recording, the amount of data for stacking was not sufficient to obtain VSGs with the desired S/N threshold). In Figure 7b, we juxtapose the smoothed velocity curve with additional meteorological data (barometric pressure, precipitation, and wind speed). The wind speed and precipitation do not have any observable correlation with the seismic velocities. The increase in the barometric pressure observed on 11 March has a weak correlation with the high-velocity excursion, but subsequent changes on 12 March do not yield a similar effect, suggesting that the barometric forcing is not a strong contributor. We should note that the meteorological measurements are not colocated with the S3 subarray and are several kilometers distant (measurements were done onboard the NOAA buoy 46,042, as denoted in Figure 1a).

DISCUSSION

The main prerequisite for the application of seafloor monitoring using dark fiber and virtual sources is that the time convergence needed to retrieve the Scholte waves or another relevant wavefield component is below or equal to the time step of the monitoring. In this study, we focus on monitoring the change in seismic velocities related to wet tidal forcings in 1 h intervals, and, as shown in Figure 4b, we are able to achieve the desired convergence by using approximately 50 min data stacks. Due to the regular behavior of the seaward AN in the analyzed frequency range (0.5–5 Hz), the increase in the S/N with the stacking time is consistent (Figure 4a) and allows us to analyze the processing steps in a traditional fashion, by tracking the progress of the S/N of the selected trace in the virtual-source data. This combination of the dark fiber and virtual-source analysis opens up the possibility of using each subsection of the dark-fiber for estimating the velocity changes in short time intervals as long as the passive recording is performed. The velocity for each time interval is estimated using dispersion spectra

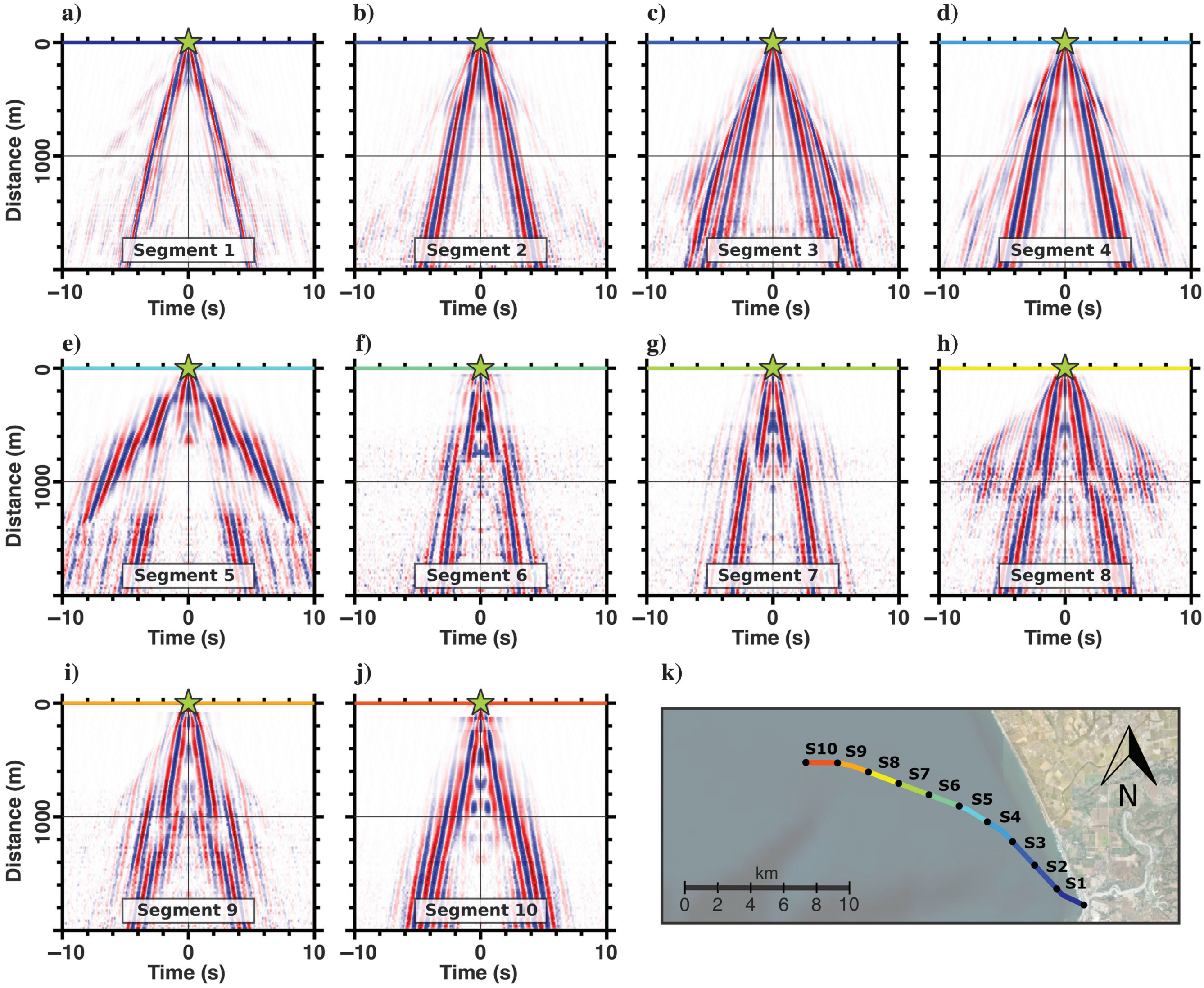

Figure 5. (a–j) Bin-stacked VSGs for 10 subarrays along the MARS DAS cable. Note the consistent retrieval of the surface-wave contribution along each segment. (k) The map indicates the location of each subarray.

computed from the improved coherency virtual-source data obtained for the given monitored time window. For this reason, the main goal of processing is to ensure that any time-dependent variations in the AN frequency spectrum related to the sources (Almagro Vidal et al., 2019; Li and Ben-Zion, 2023), the small time shifts of the virtual-source position in subsequent VSGs, and the S/N of the data used to compute the dispersion spectra are minimized. Here, we achieve this by incorporating the spectral division (equation 2), PWS, and spatial bin stacking of each 60 min set of VSGs. Specifically, the spectrally normalized crosscorrelation cancels the influence of the varying source signature (Nakata et al., 2011; Shragge et al., 2021), PWS mitigates small time shifts between the collocated traces in the VSGs retrieved for different time intervals (Schimmel and Paulssen 1997; Rodríguez Tribaldos and Ajo-Franklin, 2021), and bin stacking removes random noise by taking advantage of the dense spatial sampling (Nakata et al., 2015; Cheng et al., 2023b). All processing steps used in this study are well-established techniques. The scientific significance of this work is combining these techniques in the seafloor DAS setting to improve the temporal resolution of the seismic velocity variation to an hourly scale and thus being able to reveal the detailed variation of the seismic velocity and link it to tidal measurements.

Significance of segmentation

Linear arrays are widely used for passive monitoring studies, mainly due to their ability to efficiently use energy from sources in the stationary-phase zone (these are sources that make a dominant contribution to the surface-wave estimates; Snieder, 2004; Mehta et al., 2007; Halliday and Curtis, 2008; Chamarczuk et al., 2022; Cheng et al., 2023a; Liu et al., 2023) and the possibility of obtaining unbiased phase-velocity estimates. Furthermore, it is easier to retrieve coherent arrivals along short source-receiver offsets due to the amplitude decay of surface waves along lines of stations (Cupillard and Capdeville, 2010; Liu et al., 2023). For the preceding reasons, we argue that the most significant improvement in terms of the S/N of the retrieved surface waves and their coherence in terms of the MARS data set is achieved by the segmentation step. In our monitoring scheme, we adopt this solution and divide the submarine dark fiber into multiple short-offset (2 km) linear segments. We retrieve highly coherent VSGs consistently for each segment along the 20 km section of the MARS cable, thereby confirming the ability of the presented methodology to generate repeatable results. Based on the retrieved VSGs (Figure 5), we suggest that this methodology could also be applied to onshore dark-fiber data sets, where the presence of multiple persistent sources across the cable is common (e.g., Cheng et al., 2023b; Czarny et al., 2023). As a result of using short linear arrays, these sources could serve as a constant generator of stationary-phase surface waves for velocity monitoring. Roux et al. (2005) demonstrate that the main contribution to the EGF comes from points that lie in a stationary-phase region for the integrand of the correlation summation (i.e., for direct waves, it is a line connecting the receivers). As discussed in the “Monitoring considerations” section, there is a similarity between processing monitoring data collected using urban and seafloor dark-fiber DAS.

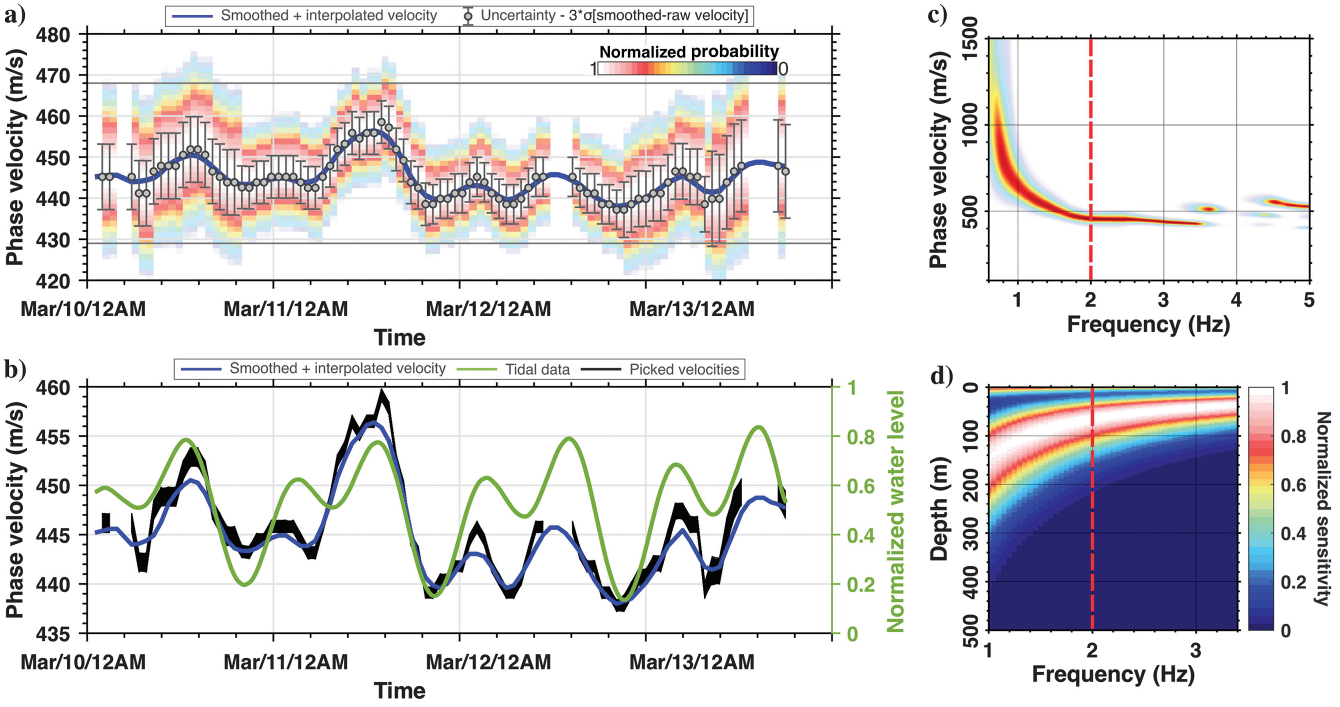

Figure 6. Seafloor dark-fiber velocity monitoring performance. (a) Estimated phase-velocity values with a sampling ratio of 1 point/h (the gray dots) and a smoothed velocity curve (the blue line). The color plot in the background corresponds to the probability density function of the values of the picked phase velocities estimated over the frequency range of 1.9 and 2.1 Hz. The error bars indicate measurement uncertainty computed as three times the standard deviation between the raw and smoothed velocity curves. (b) Smoothed phase velocities (the blue line) plotted against the raw velocity picks over the frequency range of 1.9 and 2.1 Hz, and tidal oscillation denoted by a green line. (c) Exemplary dispersion image computed using bin-stacked VSG obtained along segment 3. (d) Surface-wave sensitivity kernel of the fundamental mode surface waves used for picking the phase velocities. The dashed red line in (c) and (d) denotes the central position of the frequency bin used for picking.

Persistent sources that act as nonstationary-phase contributors for the longer arrays (e.g., 10–20 km) may be repurposed as stationary-phase sources by limiting the analysis to the shorter segments (e.g., 2 km) located approximately inline to this source, for which the stationary-phase requirement is easier to satisfy (Snieder, 2004, 2006). This analogy suggests the possibility of repurposing our monitoring scheme for urban DAS monitoring studies.

Advantages and limitations of the monitoring scheme

Another advantage of the presented monitoring scheme is the high degree of flexibility in the selection of the processing parameters tuned to a particular target: the length of the segment used for monitoring, the frequency at which the phase velocity is monitored, and the time step of monitoring, which, as mentioned previously, depends on the time convergence. Here, we focus on frequencies of approximately 2 Hz due to the high repeatability of dispersion spectrum peaks and velocity estimates in this range.

The preceding features suggest the possibility of performing monitoring at different spatial and temporal scales, constrained primarily by the available noise spectrum. We argue that due to flexibility in choosing the time step of monitoring, our method can be repurposed to track near-surface velocity responses to other environmental forcings. Past studies demonstrate seismic signatures due to temperature variations (e.g., Oakley et al., 2021), water-level changes (Rodríguez Tribaldos and Ajo-Franklin, 2021; Mao et al., 2022), and postseismic soil alteration (Wu et al., 2010; Nakata and Snieder, 2011). Perhaps the key factor is matching the monitoring epoch to the temporal variability of the monitored process; for slow variations (e.g., seasonal aquifer variability), this is not typically a challenge, but more rapid changes with periods in the minute to hour range are still at the edge of detectability due to the S/N limitations after stacking.

In general, to obtain sufficient illumination between two receivers, sufficient seismic noise sources are required to be aligned between a particular station pair (Snieder, 2004). Oceanic microseism noise tends to illuminate the array from a range of angles (Cheng et al., 2021; Guerin et al., 2022), typically covering the stationary-phase regions. Furthermore, OAN is spatially broad and relatively time-consistent as it is mainly driven by periodic tidal processes and swells (Williams et al., 2022); therefore, the methodology presented here should be applicable across a variety of dark-fiber seafloor deployments. An advantage of the PWS strategy is that the arrivals coming from sources located in the stationary-phase regions are enhanced with respect to the illumination from the nonstationary regions, and thus, with the increasing amount of stacking data over time, we progressively improve the quality of surface-wave estimates. This means that the minimum time step of monitoring could be further reduced with the application of an additional processing step, for instance, by combining SI and the beamforming technique, which was shown to be efficient in attenuating the nonstationary contributions (Gouédard et al., 2008; Cheng et al., 2016). A risk related to using shorter time intervals for monitoring is the probability of unstable surface-wave velocity estimates (e.g., Halliday and Curtis, 2008; Liu et al., 2023), as it would practically mean lowering the number of input traces for the phase coherence estimation (equation 3). This feature is related to the main limitation of the proposed monitoring approach — the potential inability to obtain coherent surface waves in the retrieved virtual-source data. For instance, a combination of local subsurface conditions, poor coupling, and the presence of strong localized noise sources (contributing to the retrieval of nonstationary arrivals) will hinder determination of the retrieved surface wave's origin (Cheng et al., 2023b). Nevertheless, provided that any coherent phases can be retrieved (this can be verified by examining the presence of surface waves in VSGs obtained using AN recordings with a length equal to the time step of the monitoring), the proposed monitoring scheme would be applicable.

Tidally modulated velocity changes

Based on the apparent correlation between velocity changes and tidal data at hourly and diurnal time scales, we hypothesize that oceanic tides are the major driving force for the observed variations. The presence of the high-amplitude anomaly between 02:00 and 17:00 on 11 March (Figure 6) suggests the presence of secondary contributions. As discussed previously, although a period of high barometric pressure overlaps with this peak, the subsequent elevations are uncorrelated, suggesting that this is not the primary driver (see the gray bars in Figure 7b). Likewise, precipitation and wind speed are uncorrelated with velocity change. One possible secondary source of variability would be changes in the AN field directionality sufficient to drive an apparent (rather

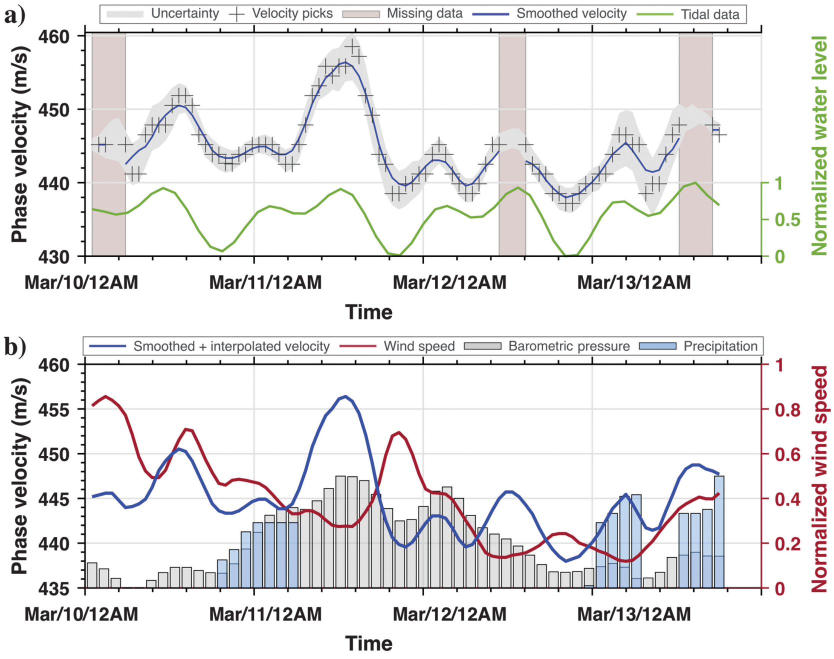

Figure 7. Comparison among the estimated phase velocities and (a) tidal data and (b) selected weather parameters. (a) Raw velocity picks for frequency 2 Hz (the black crosses) overlayed on the uncertainty (the gray shaded area) and the smoothed velocity curve (the blue line), juxtaposed with the tidal data (the green line). (b) Precipitation (the blue bars), barometric pressure (the gray bars), and wind speed (the red line) plotted against a smoothed velocity curve.

than true) velocity change; having said this, our processing strategy attempted to mitigate this effect through the use of spatial bin stacking. To assess the comparability of the resultant seismic velocity variations across different segments and their alignment with tidal variations, we have conducted an additional analysis, extending the seismic velocity analysis to all 10 segments (see Appendix A). In general, similar to segment 3 (as shown in Figure 6a), the observed velocity changes across most segments support the hypothesis that water level elevations increase the apparent velocity, albeit small phase offsets are also noticeable. However, for certain segments, not all main peaks in the tidal movement are reflected in the velocity changes, and the magnitude of the variations differs among the individual segments. This variability warrants further investigation. Nevertheless, these initial findings suggest that differences in the magnitude of the velocity variations can potentially be attributed to the higher compressibility of shallower sediments. Quantifying the stress dependence of seafloor sediments as a function of space offers another dimension for geophysical characterization beyond inversion for a static property model (Cheng et al., 2021). One hypothesis would be that zones with initially more compressible sediments (lower velocity) would exhibit larger excursions during tidal forcing. Despite this potential, our examination of the figure in Appendix A fails to reveal any discernible correlation. Notably, segment 10 presents an interesting potentially confirmatory case, as it demonstrates relatively minor velocity variations while being associated with the highest velocity in the static model.

Prior work shows that ocean tides, ocean surface gravity waves, and DAS can be used to measure quasistatic seafloor deformation, thereby opening the door to seafloor compliance measurements (Williams et al., 2022). Here, we focus on frequencies >0.5 Hz and show that oceanic tidal loading may have an influence on seismic velocities at higher frequencies. This study focuses on the methodological aspects of monitoring seafloor velocities using dark fiber, but the key result is reporting the observation of tidally modulated velocity changes of the seafloor. We hypothesize that these changes might be interpreted in terms of a combination of pore pressure and poroelastic loading, depending on the frequency of the Scholte waves used for monitoring. An oscillating ocean water level influences the effective pressure (i.e., the difference between the overburden and pore pressure) and could be incorporated into a coupled hydrologic/rock-physics model. Theoretically, static loading due to an increasing water level affects rocks at different depths equally, whereas the pore pressure should introduce a diffusive time lag. We observe that the water level elevation increases the apparent velocity, although small phase offsets are also visible; given the positive correlation, loading, rather than pore pressure diffusion, is likely the dominant effect at these frequencies. We would expect that the relative contribution of these two processes varies with depth, leading to different magnitudes in shear velocities (and, in turn, phase velocity) perturbations, particularly for higher frequency measurements sensitive to near-seafloor pore pressure transients. This issue warrants further investigation in a separate study. However, to address it partially, we examine velocity changes across different frequency bands. The results, presented in Appendix B, indicate that frequencies corresponding to shallower depths (2, 2.5, and 3 Hz) exhibit higher velocity variations (with a maximum change in phase velocity of 20.6 m/s over the analyzed four-day period) compared with frequencies associated with the deeper parts of the seafloor (10.6 m/s for 1.2 and 1.5 Hz). We anticipate that a refined poroelastic model could replicate the temporal poroelastic rock properties changes associated with ocean tides and reproduce the observed variations in seismic velocities.

CONCLUSION

Submarine dark fibers, originally installed for telecommunications purposes, are now increasingly being repurposed as dense seismic arrays due to their coverage and cost effectiveness. We have explored using this resource for Scholte wave velocity monitoring. Leveraging the power of SI and coherency improvement techniques, we develop the velocity monitoring methodology using virtual sources and submarine dark fiber. The methodology involves a systematic process of segmenting the dark fiber into subarrays, applying SI processing to the channels in each segment, and spatiotemporal stacking. Dark-fiber segments with short maximum source-receiver offset are less prone to the influence of nonstationary seismic sources and allow faster convergence of the surface-wave estimates. We verify that surface waves that are useful for monitoring may be achieved by stacking approximately 60 min of AN DAS recordings recorded by a single 2 km segment of dark fiber. Using four days of submarine dark-fiber DAS recordings, we demonstrate the systematic retrieval of highly coherent surface waves using individual segments of the cable and use one of the segments for velocity monitoring. The resulting VSGs obtained for each segment along the MARS cable consistently exhibit highly coherent arrivals, regardless of the spatial location of a given segment, thereby confirming the feasibility of this method to tackle the varying nature of the AN wavefield along the cable. The estimated velocity changes over time positively correlate with oceanic tides and further prove the reliability of the proposed methodology. Tidal loading appears to dominate over the pore pressure effects and leads to an increase in effective stress and seismic velocity. Our results demonstrate the potential of seafloor dark fiber for continuous monitoring of the response of the subsurface to ocean tide loading. The presented monitoring results are the first DAS observations of tidally modulated velocity changes on the seafloor.

ACKNOWLEDGMENTS

We extend our sincere thanks to the editors, A. Malcolm, F. Staněk, and Y. Liu, for their guidance in enhancing the quality of the paper. We especially appreciate the three anonymous reviewers for their insightful comments and constructive feedback, which improved the overall quality of our work.

DATA AND MATERIALS AVAILABILITY

Data associated with this research are confidential and cannot be released.

APPENDIX A

VELOCITY VARIATIONS ACROSS ALL SEGMENTS

Here, we investigate the performance of the seafloor dark-fiber velocity monitoring across 10 segments. In Figure A-1a, the smoothed phase velocities (blue line) are plotted against the tidal oscillation (red line), with error bars representing the minimum and maximum picked phase velocities over the analyzed frequency range (±0.1 Hz). In Figure A-1b we show the phase velocity extracted from the 2D S-wave velocity model (Cheng et al., 2021) at a depth of 75 m, alongside the mean velocities (black lines) averaged for each segment using the velocities from Figure A-1a. This comparison highlights the correspondence between the average segment-wise surface-wave velocities obtained in this study and the velocities from static 2D imaging by Cheng et al. (2021).

APPENDIX B

VELOCITY VARIATIONS ACROSS DIFFERENT FREQUENCIES AT SEGMENT 3

Here, we compare velocity variations across different frequency bands for segment S3. In Figure B-1a the surface-wave sensitivity kernel (black lines) of the fundamental mode surface waves is shown for phase velocities computed at five discrete frequencies: 1.2, 1.5, 2, 2.5, and 3 Hz. To compute sensitivity kernel, we used 1D velocity model derived from the smoothed velocity model at the

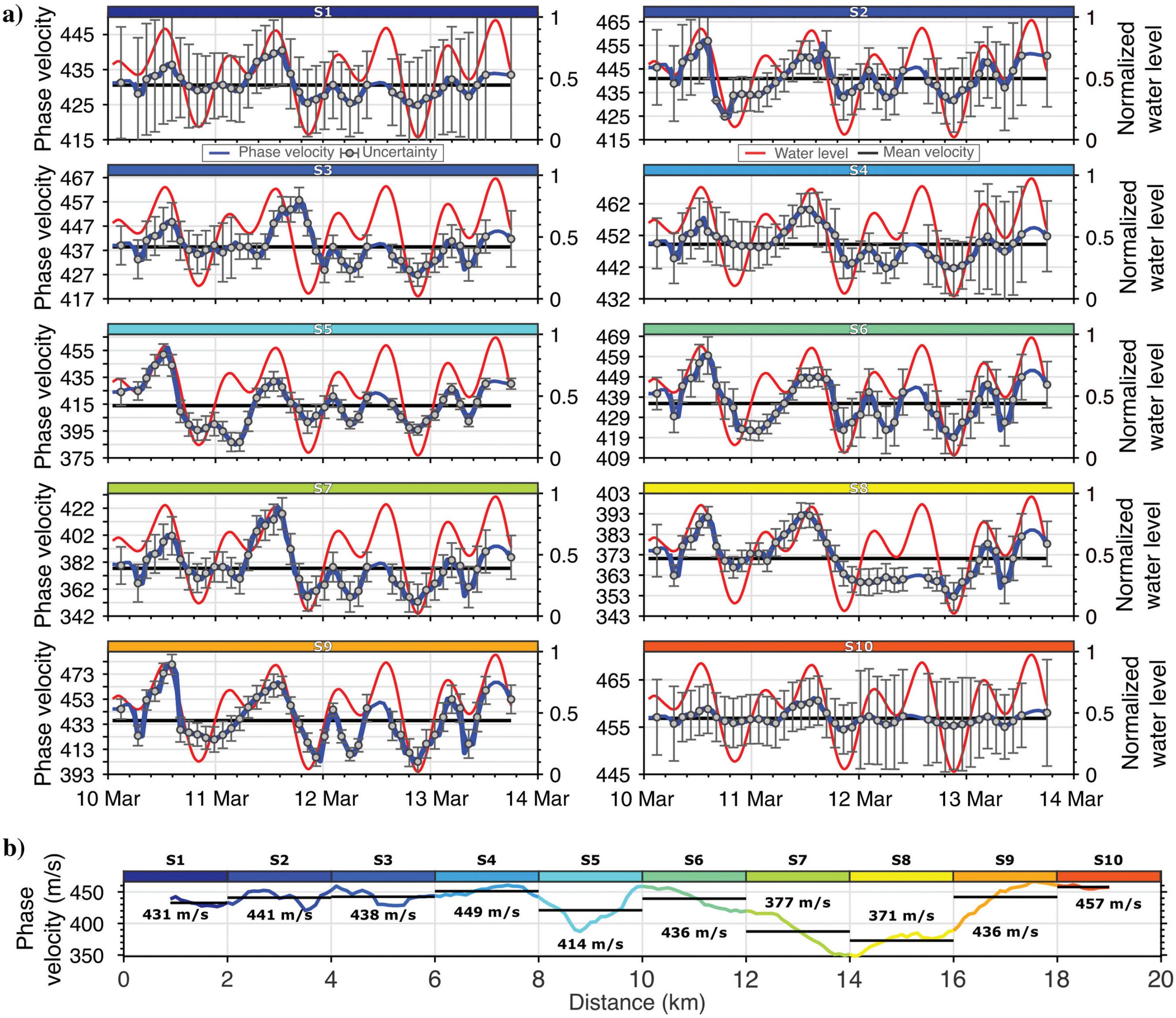

Figure A-1. The seafloor dark-fiber velocity monitoring performance of 10 segments. (a) Smoothed phase velocities (the blue line) plotted against the tidal oscillation denoted by the red line. The error bars correspond to the minimum and maximum picked phase velocity over the analyzed frequency range (analyzed frequency ±0.1 Hz). (b) Phase velocity extracted from the 2D S-wave velocity model (Cheng et al., 2021) corresponding to the depth of 75 m juxtaposed with the mean velocities (the black lines) obtained from taking the average computed for each segment using the velocities shown in (a) indicating the correspondence between the average segment-wise surface-wave velocities obtained in this study and the velocities from static 2D imaging (Cheng et al., 2021). Different colors correspond to the individual segments, as indicated by the labels above each plot.

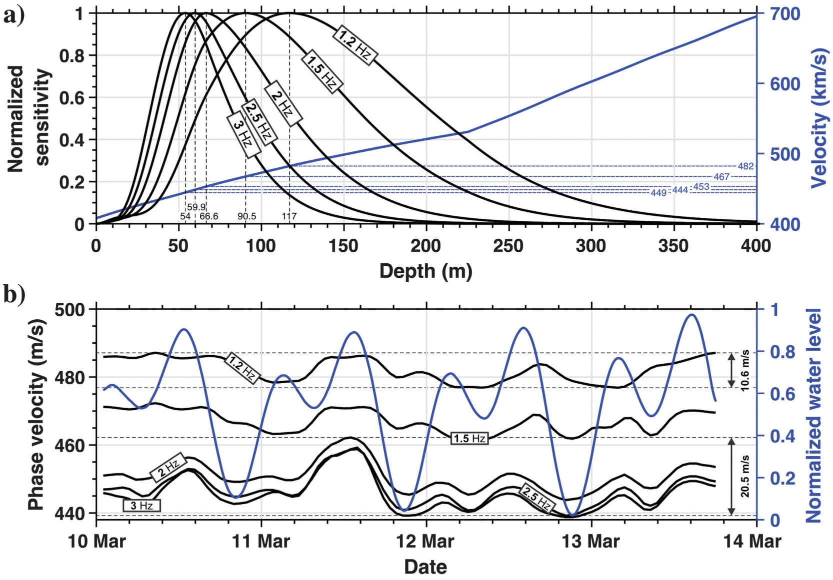

Figure B-1. Comparison of the velocity variations across different frequency bands evaluated for segment S3. (a) Surface-wave sensitivity kernel (the black lines) of the fundamental mode surface waves used for picking the phase velocities computed at five discrete frequencies: 1.2, 1.5, 2, 2.5, and 3 Hz. The blue line indicates the 1D velocity model used for computing the sensitivity kernel, corresponding to the smoothed velocity model extracted at the center of segment S3 (5 km from the shore) from the 2D velocity model by Cheng et al. (2021). (b) Smoothed phase velocities (the black line) plotted against the tidal oscillation, denoted by the blue line.

center of segment S3 (5 km from the shore) based on the 2D velocity model by Cheng et al. (2021).

REFERENCES

Ajo-Franklin, J. B., S. Dou, N. J. Lindsey, I. Monga, C. Tracy, M. Robertson, C. Ulrich, B. Freifeld, T. Daley, and X. S. Li, 2019, Using dark fiber and distributed acoustic sensing for near-surface characterization and broadband seismic event detection: Scientific Reports, **9**, 1328, doi: 10.1038/s41598-018-36675-8.

Ajo-Franklin, J. B., V. R. Tribaldos, A. Nayak, F. Cheng, R. Mellors, B. Chi, T. Wood, M. Robertson, C. Rotermund, E. Matzel, D. C. Templeton, C. Morency, K. Wu, B. Dong, and P. Dobson, 2022, The imperial valley dark fiber project: Toward seismic studies using DAS and telecom infrastructure for geothermal applications: Seismological Research Letters, **93**, 2906–2919, doi: 10.1785/0220220072.

Almagro Vidal, C., J. van der Neut, and K. Wapenaar, 2019, Reciprocity-based passive monitoring with individual sources: Geophysics, **84**, no. 2, KS29–KS38, doi: 10.1190/geo2018-0148.1.

Bakulin, A., and R. Calvert, 2004, Virtual source: New method for imaging and 4D below complex overburden: 74th Annual International Meeting, SEG, Expanded Abstracts, 112–115, doi: 10.1190/1.1845233.

Brenguier, F., D. Rivet, A. Obermann, N. Nakata, P. Boué, T. Lecocq, M. Campillo, and N. Shapiro, 2016, 4-D noise-based seismology at volcanoes: Ongoing efforts and perspectives: Journal of Volcanology and Geothermal Research, **321**, 182–195, doi: 10.1016/j.jvolgeores.2016.04.036.

Chamarczuk, M., D. Draganov, D. Quiros, and M. Malinowski, 2022, Towards adapting reverse vertical seismic profiling for ambient noise imaging with transient sources: Automatic estimation of stationary-phase receivers for improved retrieval of the interferometric Green's function: Geophysics, **87**, no. 6, KS169–KS182, doi: 10.1190/geo2021-0293.1.

Cheng, F., J. B. Ajo-Franklin, A. Nayak, V. R. Tribaldos, R. Mellors, P. Dobson, and the Imperial Valley Dark Fiber Team, 2023a, Using dark fiber and distributed acoustic sensing to characterize a geothermal system in the imperial valley, Southern California: Journal of Geophysical Research: Solid Earth, **128**, e2022JB025240, doi: 10.1029/2022JB025240.

Cheng, F., B. Chi, N. J. Lindsey, T. C. Dawe, and J. B. Ajo-Franklin, 2021, Utilizing distributed acoustic sensing and ocean bottom fiber optic cables for submarine structural characterization: Scientific Reports, **11**, 5613, doi: 10.1038/s41598-021-84845-y.

Cheng, F., J. Xia, Y. Luo, Z. Xu, L. Wang, C. Shen, R. Liu, Y. Pan, B. Mi, and Y. Hu, 2016, Multichannel analysis of passive surface waves based on crosscorrelations: Geophysics, **81**, no. 5, EN57–EN66, doi: 10.1190/geo2015-0505.1.

Cheng, F., J. Xia, and C. Xi, 2023b, Artifacts in high-frequency passive surface wave dispersion imaging: Toward the linear receiver array: Surveys in Geophysics, **44**, 1009–1039, doi: 10.1007/s10712-023-09772-1.

Cheraghi, S., D. White, D. Draganov, G. Bellefleur, J. Craven, and B. Roberts, 2017, Passive seismic reflection interferometry: A case study from the Aquistore CO_2 storage site, Saskatchewan, Canada: Geophysics, **82**, no. 3, B79–B93, doi: 10.1190/geo2016-0370.1.

Chmiel, M., A. Mordret, P. Boué, F. Brenguier, T. Lecocq, R. Courbis, D. Hollis, X. Campman, R. Romijn, and W. Van der Veen, 2019, Ambient noise multimode Rayleigh and Love wave tomography to determine the shear velocity structure above the Groningen gas field: Geophysical Journal International, **218**, 1781–1795, doi: 10.1093/gji/ggz237.

Claerbout, J. F., 1968, Synthesis of a layered medium from its acoustic transmission response: Geophysics, **33**, 264–269, doi: 10.1190/1.1439927.

Cupillard, P., and Y. Capdeville, 2010, On the amplitude of surface waves obtained by noise correlation and the capability to recover the attenuation: A numerical approach: Geophysical Journal International, **181**, 1687–1700, doi: 10.1111/j.1365-246X.2010.04586.x.

Cutillo, P. A., and J. D. Bredehoeft, 2011, Estimating aquifer properties from the water level response to earth tides: Groundwater, **49**, 600–610, doi: 10.1111/j.1745-6584.2010.00778.x.

Czarny, R., T. Zhu, and J. Shen, 2023, Spatiotemporal evaluation of Rayleigh surface wave estimated from roadside dark fiber DAS array and traffic noise: Seismica, **2**, doi: 10.26443/seismica.v2i2.247.

Daley, T., B. Freifeld, J. B. Ajo-Franklin, S. Dou, R. Pevzner, V. Shulakova, S. Kashikar, D. E. Miller, J. Goetz, J. Henninges, and S. Lueth, 2013, Field testing of fiber-optic distributed acoustic sensing (DAS) for subsurface seismic monitoring: The Leading Edge, **32**, 699–706, doi: 10.1190/tle32060699.1.

Daley, T. M., D. E. Miller, K. Dodds, P. Cook, and B. M. Freifeld, 2016, Field testing of modular borehole monitoring with simultaneous distributed acoustic sensing and geophone vertical seismic profiles at Citronelle, Alabama: Geophysical Prospecting, **64**, 1318–1334, doi: 10.1111/1365-2478.12324.

Daneshvar, M., C. Clay, and M. Savage, 1995, Passive seismic imaging using microearthquakes: Geophysics, **60**, 1178–1186, doi: 10.1190/1.1443846.

de Ridder, S., and B. Biondi, 2013, Daily reservoir-scale subsurface monitoring using ambient seismic noise: Geophysical Research Letters, **40**, 2969–2974, doi: 10.1002/grl.50594.

de Ridder, S., B. Biondi, and R. Clapp, 2014, Time-lapse seismic noise correlation tomography at Valhall: Geophysical Research Letters, **41**, 6116–6122, doi: 10.1002/2014GL061156.

Dou, S., N. Lindsey, A. M. Wagner, T. Daley, B. Freifeld, M. Robertson, J. Peterson, C. Ulrich, E. R. Martin, and J. B. Ajo-Franklin, 2017, Distributed acoustic sensing for seismic monitoring of the near surface: A traffic-noise interferometry case study: Scientific Reports, **7**, 11620, doi: 10.1038/s41598-017-11986-4.

Draganov, D., X. Campman, J. Thorbecke, A. Verdel, and K. Wapenaar, 2009, Reflection images from ambient seismic noise: Geophysics, **74**, no. 5, A63–A67, doi: 10.1190/1.3193529.

Draganov, D., X. Campman, J. Thorbecke, A. Verdel, and K. Wapenaar, 2013, Seismic exploration-scale velocities and structure from ambient seismic noise (>1 Hz): Journal of Geophysical Research: Solid Earth, **118**, 4345–4360, doi: 10.1002/jgrb.50339.

Fang, G., Y. E. Li, Y. Zhao, and E. R. Martin, 2020, Urban near-surface seismic monitoring using distributed acoustic sensing: Geophysical Research Letters, **47**, e2019GL086115, doi: 10.1029/2019GL086115.

Gouédard, P., C. Cornou, and P. Roux, 2008, Phase-velocity dispersion curves and small-scale geophysics using noise correlation slantstack technique: Geophysical Journal International, **172**, 971–981, doi: 10.1111/j.1365-246X.2007.03654.x.

Guerin, G., D. Rivet, M. van den Ende, E. Stutzmann, A. Sladen, and J. Ampuero, 2022, Quantifying microseismic noise generation from coastal reflection of gravity waves recorded by seafloor DAS: Geophysical Journal International, **231**, 394–407, doi: 10.1093/gji/ggac200.

Halliday, D., and A. Curtis, 2008, Seismic interferometry, surface waves and source distribution: Geophysical Journal International, **175**, 1067–1087, doi: 10.1111/j.1365-246X.2008.03918.x.

Issa, N. A., D. Lumley, and R. Pevzner, 2017, Passive seismic imaging at reservoir depths using ambient seismic noise recorded at the Otway CO_2 geological storage research facility: Geophysical Journal International, **209**, 1622–1628, doi: 10.1093/gji/ggx109.

Jousset, P., T. Reinsch, T. Ryberg, H. Blanck, A. Clarke, R. Aghayev, G. P. Hersir, J. Henninges, M. E. Weber, and C. M. Krawczyk, 2018, Dynamic strain determination using fibre-optic cables allows imaging of seismological and structural features: Nature Communications, **9**, 2509, doi: 10.1038/s41467-018-04860-y.

Li, G., and Y. Ben-Zion, 2023, Daily and seasonal variations of shallow seismic velocities in southern California from joint analysis of H/V ratios and autocorrelations of seismic waveforms: Journal of Geophysical Research: Solid Earth, **128**, e2022JB025682, doi: 10.1029/2022JB025682.

Lindsey, N. J., T. C. Dawe, and J. B. Ajo-Franklin, 2019, Illuminating seafloor faults and ocean dynamics with dark fiber distributed acoustic sensing: Science, **366**, 1103–1107, doi: 10.1126/science.aay5881.

Lindsey, N. J., E. R. Martin, D. S. Dreger, B. Freifeld, S. Cole, S. R. James, and J. B. Ajo-Franklin, 2017, Fiber-optic network observations of earthquake wavefields: Geophysical Research Letters, **44**, 11,792–11,799, doi: 10.1002/2017GL075722.

Lindsey, N. J., H. Rademacher, and J. B. Ajo-Franklin, 2020, On the broadband instrument response of fiber-optic DAS arrays: Journal of Geophysical Research: Solid Earth, **125**, e2019JB018145, doi: 10.1029/2019JB018145.

Lior, I., E. D. Mercerat, D. Rivet, A. Sladen, and J.-P. Ampuero, 2022, Imaging an underwater basin and its resonance modes using optical fiber distributed acoustic sensing: Seismological Research Letters, **93**, 1573–1584, doi: 10.1785/0220210349.

Lior, I., A. Sladen, D. Rivet, J. P. Ampuero, Y. Hello, C. Becerril, H. F. Martins, P. Lamare, C. Jestin, and S. Tsagkli, 2021, On the detection capabilities of underwater distributed acousting sensing: Journal of Geophysical Research: Solid Earth, **126**, e2020JB020925, doi: 10.1029/2020JB020925.

Liu, Y., J. Xia, C. Xi, H. Zhang, B. Guan, T. Dai, and L. Ning, 2023, Enhancing noise sources in stationary-phase zones for accurate phase-velocity estimation of high-frequency surface waves: Geophysics, **88**, no. 1, L1–L9, doi: 10.1190/geo2021-0696.1.

Mao, S., A. Lecointre, R. van der Hilst, and M. Campillo, 2022, Space-time monitoring of groundwater fluctuations with passive seismic interferometry: Nature Communications, **13**, 1–9, doi: 10.1038/s41467-022-32194-3.

Mao, S., A. Mordret, M. Campillo, H. Fang, and R. van der Hilst, 2020, On the measurement of seismic traveltime changes in the time–frequency domain with wavelet cross-spectrum analysis: Geophysical Journal International, **221**, 550–568, doi: 10.1093/gji/ggz495.

Mehta, K., A. Bakulin, J. Sheiman, R. Calvert, and R. Snieder, 2007, Improving the virtual source method by wavefield separation: Geophysics, **72**, no. 4, V79–V86, doi: 10.1190/1.2733020.

Melo, G., A. Malcolm, D. Mikesell, and K. van Wijk, 2013, Using SVD for improved interferometric Green's function retrieval: Geophysical Journal International, **194**, 1596–1612, doi: 10.1093/gji/ggt172.

Mordret, A., N. Shapiro, and S. Singh, 2014, Seismic noise-based time-lapse monitoring of the Valhall overburden: Geophysical Research Letters, **41**, 4945–4952, doi: 10.1002/2014GL060602.

Nakata, N., J. P. Chang, J. F. Lawrence, and P. Boué, 2015, Body wave extraction and tomography at Long Beach, California, with ambient noise interferometry: Journal of Geophysical Research: Solid Earth, **120**, 1159–1173, doi: 10.1002/2015JB011870.

Nakata, R., U.-G. Jang, D. Lumley, T. Mouri, M. Nakatsukasa, M. Takanashi, and A. Kato, 2022, Seismic time-lapse monitoring of near-surface microbubble water injection by full waveform inversion: Geophysical Research Letters, **49**, e2022GL098734, doi: 10.1029/2022GL098734.

Nakata, N., and R. Snieder, 2011, Near-surface weakening in Japan after the 2011 Tohoku-Oki earthquake: Geophysical Research Letters, **38**, L17302, doi: 10.1029/2011GL048800.

Nakata, N., R. Snieder, T. Tsuji, K. Larner, and T. Matsuoka, 2011, Shear wave imaging from traffic noise using seismic interferometry by cross-coherence: Geophysics, **76**, no. 6, SA97–SA106, doi: 10.1190/geo2010-0188.1.

Oakley, D. O., B. Forsythe, X. Gu, A. A. Nyblade, and S. L. Brantley, 2021, Seismic ambient noise analyses reveal changing temperature and water signals to 10s of meters depth in the critical zone: Journal of Geophysical Research: Earth Surface, **126**, e2020JF005823, doi: 10.1029/2020JF005823.

Obermann, A., T. Planes, E. Larose, and M. Campillo, 2013, Imaging preeruptive and coeruptive structural and mechanical changes of a volcano with ambient seismic noise: Journal of Geophysical Research: Solid Earth, **118**, 6285–6294, doi: 10.1002/2013JB010399.

Olivier, G., F. Brenguier, M. Campillo, R. Lynch, and P. Roux, 2015, Body-wave reconstruction from ambient seismic noise correlations in an underground mine: Geophysics, **80**, no. 3, KS11–KS25, doi: 10.1190/geo2014-0299.1.

Qin, L., J. H. Steidl, H. Qiu, N. Nakata, and Y. Ben-Zion, 2022, Monitoring seasonal shear wave velocity changes in the top 6 m at Garner Valley in southern California with borehole data: Geophysical Research Letters, **49**, e2022GL101189, doi: 10.1029/2022GL101189.

Qiu, H., G. Hillers, and Y. Ben-Zion, 2020, Temporal changes of seismic velocities in the San Jacinto Fault zone associated with the 2016 Mw 5.2 Borrego Springs earthquake: Geophysical Journal International, **220**, 1536–1554, doi: 10.1093/gji/ggz538.

Ratdomopurbo, A., and G. Poupinet, 1995, Monitoring a temporal change of seismic velocity in a volcano: Application to the 1992 eruption of Mt. Merapi (Indonesia): Geophysical Research Letters, **22**, 775–778, doi: 10.1029/95GL00302.

Reasenberg, P., and K. Aki, 1974, A precise, continuous measurement of seismic velocity for monitoring in situ stress: Journal of Geophysical Research, **79**, 399–406, doi: 10.1029/JB079i002p00399.

Rodríguez Tribaldos, V., and J. B. Ajo-Franklin, 2021, Aquifer monitoring using ambient seismic noise recorded with distributed acoustic sensing (DAS) deployed on dark fiber: Journal of Geophysical Research: Solid Earth, **126**, e2020JB021004, doi: 10.1029/2020JB021004.

Romanowicz, B., R. Allen, K. Brekke, L. Chen, Y. Gou, I. Henson, J. Marty, D. Neuhauser, B. Pardini, T. Taira, S. Thompson, J. Zhang, and S. Zuzlewski, 2023, SeaFOAM: A year-long DAS deployment in Monterey Bay, California: Seismological Research Letters, **94**, 2348–2359, doi: 10.1785/0220230047.

Roux, P., and Y. Ben-Zion, 2014, Monitoring fault zone environments with correlations of earthquake waveforms: Geophysical Journal International, **196**, 1073–1081, doi: 10.1093/gji/ggt441.

Roux, P., K. G. Sabra, P. Gerstoft, W. A. Kuperman, and M. C. Fehler, 2005, P-waves from cross-correlation of seismic noise: Geophysical Research Letters, **32**, L19303, doi: 10.1029/2005GL023803.

Schimmel, M., and H. Paulssen, 1997, Noise reduction and detection of weak, coherent signals through phase-weighted stacks: Geophysical Journal International, **130**, 497–505, doi: 10.1111/j.1365-246X.1997.tb05664.x.

Schuster, G. T., J. Yu, J. Sheng, and J. Rickett, 2004, Interferometric/daylight seismic imaging: Geophysical Journal International, **157**, 838–852, doi: 10.1111/j.1365-246X.2004.02251.x.

Sens-Schönfelder, C., and U. Wegler, 2006, Passive image interferometry and seasonal variations of seismic velocities at Merapi Volcano, Indonesia: Geophysical Research Letters, **33**, L21302, doi: 10.1029/2006GL027797.

Shragge, J., J. Yang, N. Issa, M. Roelens, M. Dentith, and S. Schediwy, 2021, Low-frequency ambient distributed acoustic sensing (DAS): Case study from Perth, Australia: Geophysical Journal International, **226**, 564–581, doi: 10.1093/gji/ggab111.

Sladen, A., D. Rivet, J. P. Ampuero, L. De Barros, Y. Hello, G. Calbris, and P. Lamare, 2019, Distributed sensing of earthquakes and ocean-solid earth interactions on seafloor telecom cables: Nature Communications, **10**, 1–8, doi: 10.1038/s41467-019-13793-z.

Snieder, R., 2004, Extracting the Green's function from the correlation of coda waves: A derivation based on stationary phase: Physical Review E, **69**, 046610, doi: 10.1103/PhysRevE.69.046610.

Snieder, R., 2006, The theory of coda wave interferometry: Pure and Applied Geophysics, **163**, 455–473, doi: 10.1007/s00024-005-0026-6.

Snieder, R., and M. Hagerty, 2004, Monitoring change in volcanic interiors using coda wave interferometry: Application to Arenal volcano, Costa Rica: Geophysical Research Letters, **31**, L09608, doi: 10.1029/2004GL019670.

Snieder, R., M. Miyazawa, E. Slob, I. Vasconcelos, and K. Wapenaar, 2009, A comparison of strategies for seismic interferometry: Surveys in Geophysics, **30**, 503–523, doi: 10.1007/s10712-009-9069-z.

Spica, Z., K. Nishida, T. Akuhara, F. Pétrélis, M. Shinohara, and T. Yamada, 2020, Marine sediment characterized by ocean-bottom fiber-optic seismology: Geophysical Research Letters, **47**, e2020GL088360, doi: 10.1029/2020GL088360.

Spica, Z. J., J. Castellanos, L. Viens, K. Nishida, T. Akuhara, M. Shinohara, and T. Yamada, 2022, Subsurface imaging with ocean-bottom distributed acoustic sensing and water phases reverberations: Geophysical Research Letters, **49**, e2021GL095287, doi: 10.1029/2021GL095287.

Stork, A., C. Allmark, A. Curtis, J. M. Kendall, and D. White, 2018, Assessing the potential to use repeated ambient noise seismic tomography to detect CO_2 leaks: Application to the Aquistore storage site: International Journal of Greenhouse Gas Control, **71**, 20–35, doi: 10.1016/j.ijggc.2018.02.007.

Thangraj, J., and J. Pulliam, 2021, Towards real-time assessment of convergence criteria in seismic interferometry: Selective stacking of cross-correlations at the San Emidio geothermal field: Journal of Applied Geophysics, **193**, 104426, doi: 10.1016/j.jappgeo.2021.104426.

Vasconcelos, I., and R. Snieder, 2008, Interferometry by deconvolution: Part 1 — Theory for acoustic waves and numerical examples: Geophysics, **73**, no. 3, S115–S128, doi: 10.1190/1.2904554.

Viens, L., M. Perton, Z. Spica, K. Nishida, T. Yamada, and M. Shinohara, 2023, Understanding surface wave modal content for high-resolution imaging of submarine sediments with distributed acoustic sensing: Geophysical Journal International, **232**, 1668–1683, doi: 10.1093/gji/ggac420.

Wapenaar, K., 2003, Synthesis of an inhomogeneous medium from its acoustic transmission response: Geophysics, **68**, 1756–1759, doi: 10.1190/1.1620649.

Wapenaar, K., and J. Fokkema, 2006, Green's function representations for seismic interferometry: Geophysics, **71**, no. 4, SI33–SI46, doi: 10.1190/1.2213955.

Wapenaar, K., J. Thorbecke, and D. Draganov, 2004, Relations between reflection and transmission responses of three-dimensional inhomogeneous media: Geophysical Journal International, **156**, 179–194, doi: 10.1111/j.1365-246X.2003.02152.x.

Weaver, R. L., and O. I. Lobkis, 2001, Ultrasonics without a source: Thermal fluctuation correlations at MHz frequencies: Physical Review Letters, **87**, 134301, doi: 10.1103/PhysRevLett.87.134301.

Webb, S. C., 1986, Coherent pressure fluctuations observed at two sites on the deep sea floor: Geophysical Research Letters, **13**, 141–144, doi: 10.1029/GL013i002p00141.

Webb, S. C., X. Zhang, and W. Crawford, 1991, Infragravity waves in the deep ocean: Journal of Geophysical Research, **96**, 2723–2736, doi: 10.1029/90JC02212.

Wegler, U., and C. Sens-Schönfelder, 2007, Fault zone monitoring with passive image interferometry: Geophysical Journal International, **168**, 1029–1033, doi: 10.1111/j.1365-246X.2006.03284.x.

Williams, E. F., M. R. Fernandez-Ruiz, R. Magalhaes, R. Vanthillo, Z. Zhan, M. Gonzalez-Herraez, and H. F. Martins, 2019, Distributed sensing of microseisms and teleseisms with submarine dark fibers: Nature Communications, **10**, 1–16, doi: 10.1038/s41467-019-13262-7.

Williams, E. F., Z. Zhan, H. F. Martins, M. R. Fernández-Ruiz, S. Martín-López, M. González-Herráez, and J. Callies, 2022, Surface gravity wave interferometry and ocean current monitoring with ocean-bottom DAS: Journal of Geophysical Research: Oceans, **127**, e2021JC018375, doi: 10.1029/2021JC018375.

Wu, C., Z. Peng, and Y. Ben-Zion, 2010, Refined thresholds for non-linear ground motion and temporal changes of site response associated with medium-size earthquakes: Geophysical Journal International, **182**, 1567–1576, doi: 10.1111/j.1365-246X.2010.04704.x.

Yang, J., and J. Shragge, 2023, Long-term ambient seismic interferometry for constraining seasonal subsurface velocity variations in urban settings: A distributed acoustic sensing (DAS) case study: Geophysical Journal International, **234**, 1973–1984, doi: 10.1093/gji/ggad181.

Yu, C., Z. Zhan, N. J. Lindsey, J. B. Ajo-Franklin, and M. Robertson, 2019, The potential of DAS in teleseismic studies: Insights from the Goldstone experiment: Geophysical Research Letters, **46**, 1320–1328, doi: 10.1029/2018GL081195.

Zhan, Z., 2019, Distributed acoustic sensing turns fiber-optic cables into sensitive seismic antennas: Seismological Research Letters, **91**, 1–15, doi: 10.1785/0220190112.

Biographies and photographs of the authors are not available.